Untethered Micro-Actuators for Autonomous Micro-Robot Locomotion: Design, Fabrication, Control, and Performance

Bruce R. Donald*, Christopher G. Levey**, Craig D. McGray***, Daniela Rus‡, and Mike Sinclair†

Dartmouth Departments of Computer Science, Chemistry, and Biological Sciences
Dartmouth Thayer School of Engineering
Microsoft Research

Abstract. This paper presents a micro-actuator that operates free of any physically restraining tethers. We show how capacitive coupling can be used to deliver power to untethered MEMS (micro-electromechanical systems) devices, independently of their position and orientation. Our novel power delivery and actuation mechanisms are designed for use in autonomous mobile robots whose dimensions can be measured in tens to hundreds of micrometers. Test devices utilizing these mechanisms have been fabricated at scale using MEMS technology, and have been shown capable of untethered locomotion at speeds exceeding 1.5 mm/sec. The corresponding speed, scaled to a car-sized robot would be over 100 km/hr. The possibility of autonomous (untethered) microactuators and microrobots less than 80 μm in length opens the door to novel applications in distributed and parallel robotics

Scratch-drive actuators (SDAs) [1,2] are capable of both high speed and nanometer-scale precision, making them a promising choice for the actuators of mobile microrobots. We developed a novel kind of SDA that walks without the physically-restraining electrical tethers, rails, stators, or springs required in previous work. Our power delivery mechanism operates through a capacitive coupling with a silicon substrate that underlies the mobile device. This allows the device actuation mechanism to use electrostatic forces without requiring any physical connection or wire that would restrain the motion of the device. Through appropriate design of the substrate wiring and actuator geometries, the power delivered to the device can be shown to be independent of the device's position and orientation. For this reason, this power delivery mechanism is appropriate for fully two-dimensional (x, y) and (x, y, θ) mobile microrobots.

1 Introduction

Over the past ten years, there has been a great deal of interest in pushing the limits of mobile robot technology to smaller and smaller sizes [3–23]. However, there remains a large gap

* Corresponding author: Dartmouth Computer Science Department, Dartmouth Chemistry Department, and Dartmouth Department of Biological Sciences, 6211 Sudikoff Laboratory, Hanover, NH 03755 USA (e-mail: brd@cs.dartmouth.edu).

** Dartmouth Thayer School of Engineering, Hanover, NH 03755 USA.

*** Dartmouth Computer Science Department, Hanover, NH 03755 USA.

† Microsoft Research, Redmond, WA USA.

P. Dario and R. Chatila (Eds.): Robotics Research, STAR 15, pp. 502–516, 2005.
© Springer-Verlag Berlin Heidelberg 2005

between the size of the smallest actuators and manipulators, and the size of the smallest *mobile* devices. For example, while a thin film robot arm has been built at the sub-millimeter scale [24], state of the art miniature mobile robots are still in the millimeter to centimeter range. In large part, this difference in scale is due to the problem of how to deliver power to a microscopic autonomous system, without restraining its motion with physical tethers such as rails, stators, or springs.

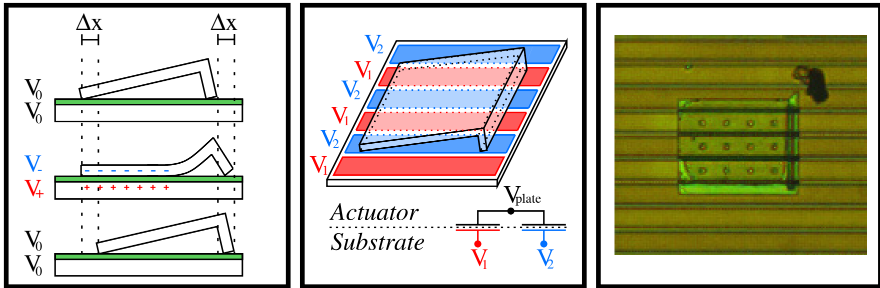

Fig. 1.1. Left: A schematic of the operation of a scratch drive actuator [1,2]. **Center:** A schematic of the capacitively-coupled power delivery mechanism. The voltage induced on the actuator, V_{plate}, is approximately the mean of the voltages applied to the electrodes (V_1 and V_2). **Right:** An optical micrograph of an untethered scratch drive actuator atop the insulating electrodes that provide it with power.

In previous work, the power delivery problem has been approached in a number of ways. Energy has been provided to actuators through vibration [14], through photo-thermal transduction [3,4], and electrically through gold bonding wire [7,12,13,15]. These approaches produced microrobots with sizes between 1.5 mm and 3 cm. We propose the use of a capacitive coupling for electrostatic power delivery, that allows fabrication and control of untethered actuators of less than 80 μm in length, while requiring a minimum of assembly, all of which can be automated on-chip. The actuators have demonstrated the ability to assist in their own assembly, to push small objects, and have achieved operating speeds in excess of 1.5 mm/sec.

The possibility of autonomous (untethered) microactuators and microrobots less than 80 μm in length opens the door to a number of novel applications in distributed and parallel robotics. For example, we have shown that our microactuators are strong enough to push small objects (such as organic and silicon debris on the wafer). The planning and control of micro-pushing strategies could build on the mechanics of planar pushing manipulation [25] to extend our distributed, multi-robot pushing protocols [26]. As another example, in meso-scale self-assembly (e.g., [27]), the assembly constituents have traditionally been *passive* participants in the complex dynamical system that drives the self-assembly process. Consequently, to date, the components of a self-assembled system have, almost always, been more like manipulanda, and less like robots. Autonomous (untethered) microrobots would enable a self-assembly paradigm in which the pieces of a self-assembling system could be *active* participants in their assembly. In princple, autonomous microrobotic and microactuator components could serve a more active role in self-assembly, analogous to the biopolymers, enzymes, and cells observed in natural self-assembling systems. Applications are also foreseen in self-reconfiguring robotics [28], in which a collection of microrobots could change shape to perform different tasks.

A host of practical challenges remain before such applications are reduced to practice. However, we are optimistic about the potential of these MEMS devices because of our results on (a) speed/performance and (b) ease of fabrication. In particular, our actuators are quite fast: the corresponding speed, scaled to a car-sized robot would be over 100 km/hr. Hence, in principle, these microscopic pushing, manipulation, self-assembly, and self-reconfiguration tasks could be performed efficiently. Finally, even though the fabrication process was difficult to characterize and refine, it can now be easily and rapidly replicated by any laboratory with access to a standard MEMS multi-project wafer process such as the public CRONOS PolyMUMPS process [29].

2 Background – Tethered Scratch Drive Actuators

A scratch drive [13,1,2,30,31] is a type of direct-drive actuator that operates through electrostatic attraction. It is composed of a thin polysilicon plate with a bushing at the front end. The plate is typically in the range of 80 μm on a side, and 1-2 μm thick. The bushing height is typically in the 1-2 μm range. The plate is electrically connected to a voltage source through the same spring tether, rotor, or rail that provides it with physical connection to the substrate. The substrate is grounded, and insulated from the scratch drive by a thin layer of dielectric.

The scratch drive operates as shown in Figure 1.1. When a voltage is applied between the polysilicon plate and the substrate beneath it, the plate is drawn down into contact with the dielectric layer. Since the front of the plate is supported by the bushing, strain energy is stored in the plate, and the edge of the bushing is pushed forward. When the voltage is removed, the strain is released and the scratch drive plate snaps back to its original shape, slightly in front of where it began. When a periodic pulse is applied, this cycle is continuously repeated, and the scratch drive moves forward in a step-wise manner.

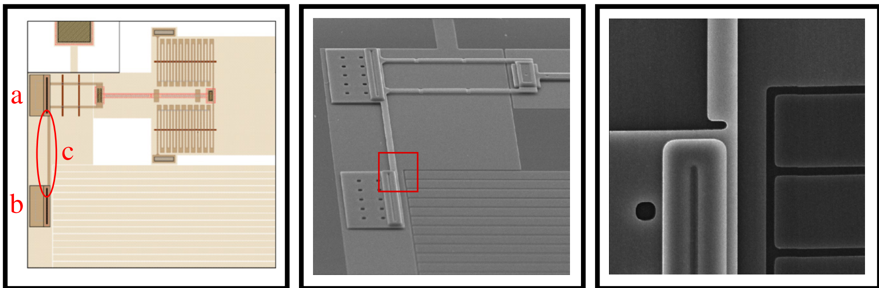

Fig. 1.2. Operation of the self-release mechanism. The assisting spring-tethered scratch drive (a) moves forward while the target actuator for the release operation (b) holds down to the substrate by electrostatic attraction. The restraining beam (c) breaks at the score mark. **Left:** CAD Layout of the mechanism. **Center:** Electron micrograph of the self-release setup. **Right:** Close-up of the score mark where the restraining beam joins the target actuator.

The typical average step size achieved by a scratch drive actuator is around 30 nm. This makes the scratch drive an ideal actuation mechanism for thin film microrobots. It allows for high precision of movement, while providing the possibility of high speeds when the actuators are driven at large frequencies.

3 Power Delivery Mechanism

We designed, fabricated, controlled, and tested the first untethered version of the scratch drive actuator. In a *tethered* scratch drive actuator, the power is provided through the same connection that attaches the device to the substrate. To build *untethered* devices, we require a different power delivery mechanism.

One solution is to provide power through a capacitive coupling. This type of power delivery mechanism has been successfully used in the development of gas-lubricated micromotors [32] and has been proposed for use in flying insect-model microrobots [19].

To use capacitively-coupled power for mobile microrobots, the operating environment must be structured so that a constant voltage is maintained as the actuator changes its position and orientation. To do this, we cover the surface of the substrate with a sequence of insulated electrodes, as shown in Figures 1.1.

When power and ground are applied to adjacent electrodes, an untethered scratch drive actuator placed in any orientation on these electrodes forms the capacitive circuit shown in Figure 1.1. The potential applied to the scratch drive plate is the potential on the wire between the two capacitors in this circuit:

$$V_{plate} = \frac{V_1 C_1 + V_2 C_2}{C_1 + C_2} \tag{1.1}$$

where V_1 and V_2 are the applied voltages, and C_1 and C_2 are the capacitances.

The capacitances C_1 and C_2 are proportional to the area of overlap between the scratch drive plate and the low-voltage and high-voltage electrodes, respectively. If the dimensions of the actuator greatly exceed the width of each electrode, then the area of high-voltage overlap will always be maintained roughly equal to the area of low-voltage overlap. So, the potential induced between the actuator and any of the electrodes beneath it will be roughly half that applied between the electrodes themselves, regardless of the position and orientation of the drive.

Charging of this circuit produces the electrostatic attraction between the scratch drive and the electrodes, which in turn bows the actuator's plate downward and its bushing forward, causing incremental forward motion.

We have verified this power delivery mechanism by driving untethered scratch drive actuators in a variety of directions, as shown in Figure 1.3. In particular, we have successfully driven these actuators in parallel, perpendicular, and diagonal directions relative to the underlying electrodes. In addition, the power delivery mechanism was demonstrated to be robust with respect to the electrode width. Actuators were even observed to continue operating (albeit at reduced speed) after walking off of the main Poly0 electrode panels (18 μm width, 20 μm pitch) onto the connecting Poly0 wires (6 μm width, 20 μm pitch) that deliver power to the main electrodes from the bonding pads (See Table 1.2, entries marked †).

4 Device Design

The major components of the untethered actuators are the scratch drive plates, the bushings, and the electrodes. In addition, we must fabricate anchors that provide physical connection of the actuators to the substrate during processing, and sacrificial tethers that connect the actuators to the anchors. Removal of the sacrificial tethers will be described in Section 1.6.

In order to leverage existing MEMS infrastructure, we have fabricated the actuators using the PolyMUMPs multi-project wafer process provided by Cronos Integrated Microsystems

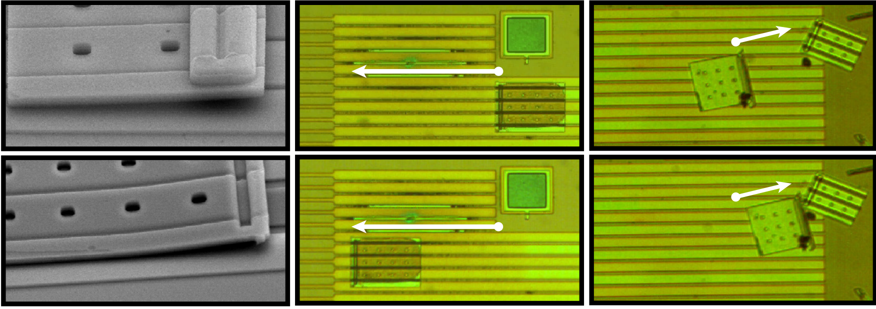

Fig. 1.3. Left: Scanning electron micrographs of untethered scratch drive actuators with $1.5\ \mu m$ (top) and $0.75\ \mu m$ (bottom) bushings. **Center:** Frames extracted from video of a device in motion show an untethered actuator moving parallel to the electrodes. **Right:** Extracted video frames show a device moving diagonally with respect to the electrodes. The motion of untethered scratch drive actuators is independent of their orientation.

[29]. This process provides an unpatternable sheet of silicon nitride that electrically isolates the devices from a silicon substrate, and three patternable layers of conductive polysilicon. Of these three structural layers, Poly0 is permanently fixed to the substrate, while Poly1 and Poly2 can be released through a sacrificial etch that occurs at the end of the processing sequence. Phosphosilicate glass serves as the the sacrificial material, and is laid down twice over the course of the process; once between Poly0 and Poly1, and again between Poly1 and Poly2. These two layers of phosphosilicate glass are referred to as First Oxide and Second Oxide, respectively. Connection between Poly0 and Poly1 can be obtained through the Anchor1 patterned etch, and connection between Poly1 and Poly2 is obtained through the Poly1-Poly2-Via etch. Direct connection between Poly0 and Poly2 can be obtained through the use of the Anchor2 etch. Surface topology of the releasable polysilicon layers can be controlled through a $0.75\ \mu\text{m}$ patternable timed etch of First Oxide, called Dimple Etch. Lastly, a patternable metal layer is provided on top of Poly2. However, due to post-processing constraints described in Section 1.5, we do not use this last layer in our designs.

4.1 Electrode Design

Electrodes are fabricated from the Poly0 layer, and are designed as long, narrow strips to make it easy to cover a large area without complicated wiring. The electrodes are $18\ \mu\text{m}$ wide, with a $2\ \mu\text{m}$ inter-electrode separation. That is to say, the electrode pitch is always maintained at $20\ \mu\text{m}$. When wires need to cross in order to provide different signals to adjacent electrodes, electrical bridges are introduced on the Poly1 layer.

4.2 Scratch Drive Design

It is important that the voltage delivered to the actuator be approximately independent of the actuator's position and orientation (see Section 1.3). If the electrodes are very thin relative to the dimensions of the actuator, this will always be the case. However, since the scratch drive actuators must have plate dimensions on the order of $100\ \mu\text{m}$, and since the electrode pitch is $20\ \mu\text{m}$, it is possible for the voltage to vary somewhat. The amount that the voltage can vary depends on the dimensions of the scratch drive. The variation in the voltage applied

to the actuator can be minimized if the length and width of the scratch drive are both even integer multiples of the electrode pitch, as shown in Figure 1.4.

The scratch drive plates are fabricated from a single sheet of Poly2 that is either 80 or 120 $\mu\mathrm{m}$ wide, and either 40, 60, 80, or 100 $\mu\mathrm{m}$ long. This allows the plate dimensions to be (in all but the 60 $\mu\mathrm{m}$ case) even integer multiples of the electrode pitch. In this way, the power delivered to the devices can be maintained at a constant level, regardless of their position and orientation. The plates are patterned with holes at 30 $\mu\mathrm{m}$ intervals to make the underlying oxide accessible to the etchant during sacrificial release.

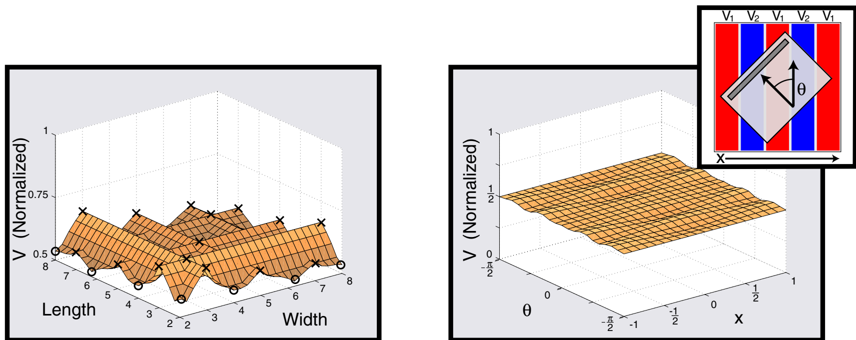

Fig. 1.4. Plate design for untethered scratch drive actuators. The size of an untethered scratch drive actuator relative to its underlying electrodes can have a significant effect on the voltage delivered to the device. Ideally, this voltage will be independent of the actuator's position and orientation. The length and width of the actuator can be chosen to make this approximately true. **Left:** The maximum possible deviation in voltage for an actuator in any position or orientation. The maximum normalized plate voltage $(V_{plate} - V_1) / (V_2 - V_1)$ is plotted against the actuator's length and width (expressed as multiples of the electrode width). Maximum deviation from the mean voltage (normalized voltage = 0.5) is small for actuators that are large compared to the electrode width, and for actuators whose sides are even integer multiples of the electrode width. Good locations in the design space are marked here with 'O's, and locations leading to highly-variable power delivery are marked with 'X's. **Right:** shows the normalized plate voltage for one of the actuator designs that we fabricated, as a function of position and orientation defined relative to the electrodes as shown in the inset. This actuator has a length of 120 μm, a width of 80 μm, and lies above a series of 20 μm-wide electrodes. The normalized voltage is approximately 0.5 for all poses, with a maximum deviation of 0.0158.

Two different scratch drive bushings were designed with heights of 0.75 $\mu\mathrm{m}$ and 1.5 $\mu\mathrm{m}$. The shorter bushings were defined by conformalities in the Poly2 layer resulting from the Dimple Etch pattern. Taller bushings combined a Dimple Etch conformality with a sheet of Poly1 anchored to the Poly2 layer. In these latter designs, the Poly1-Poly2-Via etch adds an additional 0.75 $\mu\mathrm{m}$ to the bushing height.

4.3 Sacrificial Tether Design

Substrate anchors are formed from a sheet of Poly2 connected by the Anchor2 etch to an underlying sheet of Poly0. The scratch drive actuators are connected to these anchor points by

means of sacrificial tethers composed of simple beams on the Poly2 layer. These beams are notched where they join the actuators so that, when under flexure, they concentrate stress at the joint. This way, the tethers break cleanly, and do not leave a significant flange of material on the actuators after release.

4.4 Component Integration

If the actuators are fabricated directly above the electrodes, they will exhibit conformalities corresponding to the inter-electrode gaps. For this reason, it is best to fabricate the actuators above a flat region of the die. The actuator must then be moved into position above the electrodes at some point prior to operation. Section 1.6 presents a way that this placement can be performed in an automated fashion.

5 Fabrication Process

Following the sacrificial etch that completes the PolyMUMPs process, there is no layer of insulator between the Poly2 layer (on which we fabricate the actuators) and the Poly0 layer (on which we fabricate the electrodes). For power to be delivered to the devices through the process described in Section 1.4, we must add an insulating layer *between* Poly0 and Poly2. In this section, we describe a post-processing sequence for providing this intermediate insulating layer on released polysilicon microstructures.

Of course, when devices are received from the PolyMUMPS process, there is already a layer of silicon dioxide between the Poly0 and Poly2 layers – namely, the first and second sacrificial oxides. However, these layers must be removed in order to release the devices. A portion of this oxide must be replaced to provide insulation, but the devices must remain released.

We use wet thermal oxidation to grow a new layer of insulation around the released devices. This leads to a number of important considerations.

First, all released devices must be supported above the surface of the substrate, so as to expose them to the oxidant through the carrier gas, and prevent them from fusing to underlying layers during oxidation. It is very important, therefore, not to allow any devices to be pulled into contact with the substrate by the surface tension that occurs during the drying process that follows sacrificial release. For this reason, we dry the devices using super-critical CO_2. Second, there must be no gold (or other high-mobility materials) on the die. Gold will diffuse through the nitride layer during oxidation, causing short circuits. For this reason, the PolyMUMPS Metal layer is not used. Electrical wiring is done with the Poly0 layer, and contact pads are fabricated from stacks of all three polysilicon layers. Third, a means must be provided for making electrical contact with the devices once processing is complete. During oxidation, the contact pads will become insulated, and this insulator must be subsequently removed. We have done this by using photolithography followed by a buffered hydrofluoric acid wet chemical etch. Narrow channels between the released devices and the substrate provide opportunities for residual photoresist scum from this process step to adhere to the die. Care must be taken, as described below, to avoid this problem.

Because the oxidation step is performed *after* sacrificial release, oxide will grow on both the top and the underside of all released devices. However, since the channel between a released device and the substrate is only $2.75\ \mu\text{m}$ wide, oxidants are delivered more slowly to the underside of a device than to its top surface. As a result, oxide growth is uneven on the two surfaces. Stress will not be balanced on the top and bottom of the device, resulting

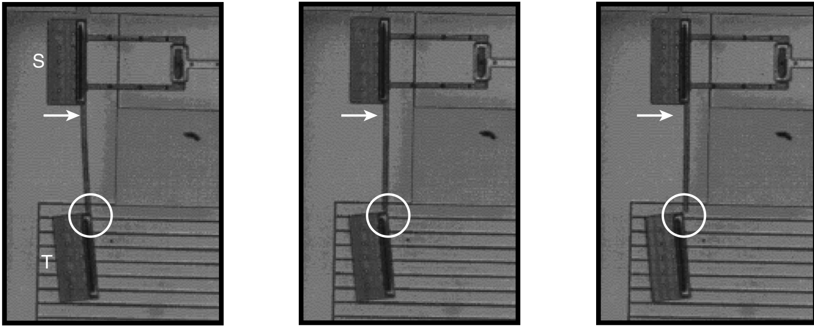

Fig. 1.5. Frames captured from video footage of the self-release process. **Left:** The target drive (T) holds down electrostatically to the substrate. **Center:** The assisting drive (S) continues actuating. **Right:** The tether snaps at the score mark, releasing the target actuator.

in out-of-plane curvature. A slow oxidation at low temperature resolves this problem. Our devices were oxidized at 550° C for a duration of 8 days. Oxide thickness data were obtained through ellipsometric measurements of n-type silicon test wafers that shared the furnace with the PolyMUMPs dice. Using this process, the curvature produced in the released structures is negligible.

Following oxidation, the dice undergo photolithography to open contact holes above the pads. The dice are first spin-coated in hexamethyl disilazane (HMDS) to promote adhesion of the photoresist to the oxidized surfaces, and then in Shipley 1813 photoresist (Shipley Company, Marlborough, MA) and exposed. The pattern is then transferred into the oxide with a 10:1 buffered hydrofluoric acid wet chemical etch.

After etching contact holes, the photoresist is removed by a 10-minute soak in 60° C ACT positive photoresist stripper (Ashland-ACT, Easton, PA) using gentle agitation. This removes the top coat of photoresist, and also any resist that has been trapped in the $2.75\ \mu\mathrm{m}$ channel between the released devices and the underlying substrate. This is followed by a triple rinse in deionized water to wash away the solvent. The use of hot ACT solvent for photoresist removal at this step dramatically reduces stiction difficulties in the completed devices. The dice are transferred to an ethanol bath, and dried once again in super-critical CO_2. To complete the process, the dice are then wire-bonded to ceramic leadless chip carriers. Because the contact pads are bare silicon, wire bonding must be performed at a temperature of 120° C to obtain adequate adhesion to the pads. At this point, the chemical processing is complete, and it remains only to remove the tethers that were used to hold the devices above the substrate throughout the fabrication process. This mechanical release step is described in the next section.

6 Mechanical Release

Following the post-processing sequence described in Section 1.5, the actuators are still attached to the substrate by physical tethers. These tethers, shown in Figure 1.2, are strong enough to withstand the rigors of the fabrication process, but are designed to break in a controlled fashion under a small amount of mechanical pressure.

We have performed controlled mechanical release of the actuators in two ways. First, we have released the devices manually, with a pair of microprobes. This is simple to do, and is quite practical for research purposes, where the number of actuators to be released is small. In a production setting, where the number of actuators would be much larger, an automated solution would be required. Therefore, we have developed a means by which the actuators can perform their own electromechanical release, requiring only an electrical signal from the operator.

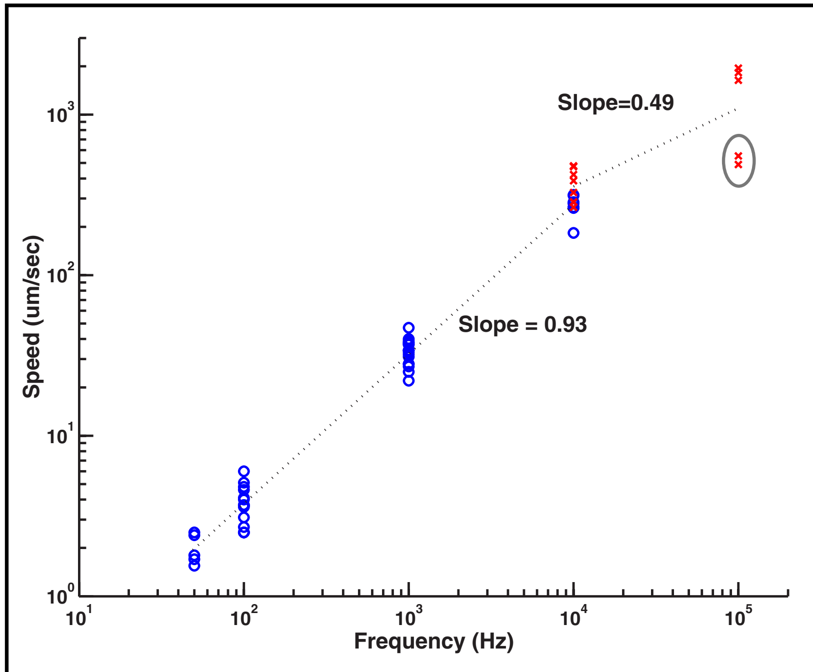

Fig. 1.6. Actuator speed as a function of frequency. Control of untethered micro-actuators is possible at a wide range of frequencies and speeds. Data points marked with an 'o' (in blue) reflect average speeds. Data points marked with a dot (in red) reflect maximum inter-frame speeds. Circled data points reflect motion that occurred off of the intended electrodes and above (much thinner) electrical wiring. The slope of the plot shown in log-log space above, reflects a slight decrease in the step size of the actuators as the frequency increases across four orders of magnitude.

6.1 Manual Release

We have released the devices manually, with a pair of microprobes. The first probe applies downward pressure on the scratch drive plate, creating a large area of contact with the substrate and immobilizing the actuator. The second microprobe applies lateral pressure on the tether.

The stress from this action is concentrated in the score mark that was fabricated in the tether, resulting in fracture at the desired location.

Once the actuator has been released, it must be positioned above a sheet of electrodes before operating.[1] This process is performed manually with a microprobe. Since the power delivery mechanism is independent of position and orientation, very little precision is required in this placement step. Once the actuators have been mechanically released and placed on top of the electrodes, they are fully operable.

6.2 Automated Self-Release

For purposes of batch fabrication, we would like to be able to perform this assembly process in an entirely automated fashion. The process has two steps. The actuator is operated to walk onto an electrode-covered area of the substrate, and is then electromechanically released from its fabrication tethers. The setup for this assembly process is shown in Figure 1.2.

We used a spring-tethered assisting scratch drive actuator to pull the target actuator into position above a set of electrodes. The two actuators are attached at the bushing by a polysilicon beam, which provides both physical and electrical connection. A voltage is applied to both actuators through the spring that anchors the assisting actuator to the nitride-coated substrate.

Initially, both actuators lie over a flat sheet of (oxide-insulated) Poly0, which is connected to ground. A periodic voltage is applied between the actuators and the underlying Poly0 sheet, in order to cause forward motion of both scratch drives. Since the two scratch drives have the same length, width, and bushing height, they move forward at the same speed.

As the actuators move forward, the path of the assisting actuator continues to be paved with a single flat sheet of oxide-insulated Poly0. The path of the target actuator, on the other hand, quickly changes into a sheet of electrode panels. These electrodes are all held at ground potential, so that the motion of both scratch drives continues as before. However, once the target actuator has moved completely onto the electrode surface, a DC voltage is applied to the electrode panels. In this way, as the potential of the scratch drives oscillates between high-voltage and ground, there is always an attractive force between the target actuator and the surface beneath it. So, the target actuator holds down electrostatically to the substrate, thereby causing friction, which immobilizes the actuator with respect to both translation and rotation. The assisting actuator continues moving as before.

As the assisting actuator continues to move, it bends the beam that connects the two actuators. The resulting stress is concentrated in the score mark that was fabricated where the beam joins the target actuator, and the beam breaks at the desired location. Frames captured from video footage of this self-release process are shown in Figure 1.5.

At this point, the assembly of the target actuator is complete. A periodic potential applied to the underlying electrodes results in untethered actuation.

7 Device Performance

Untethered scratch drive actuators are operable over a wide range of parameter values. We operated untethered scratch drives that were 80-120 μm wide, between 40 μm and 100 μm long, and had bushing heights of 0.75 μm and 1.5 μm. Untethered actuators from two different PolyMUMPs runs were observed to have correct operation.

[1] If the actuator were fabricated directly above the electrodes, it would exhibit conformalities above the inter-electrode gaps.

Table 1.1. Average Speed as a Function of Frequency. Left: Plate Voltage = 50 V. Right: Plate Voltage = 60 V.

Device	Length (μm)	Width (μm)	Speed (μm/sec) 50 Hz	100 Hz	1 kHz	10 kHz
1	80	100		6.0	33	
2	80	100		4.6	25	
3	100	80		5.1	34	
4	100	80			38	
5	100	80	1.8	4.0	37	
6	100	80	1.7	3.7	39	
7	100	80	2.4	4.8	38	
8	100	80			32	262
9	100	80	2.5		28	279
10	100	80	3.1		40	
11	100	100			47	
Mean			**2.3**	**4.7**	**35.5**	**270.5**
Std. Dev.			**0.6**	**0.8**	**6.1**	**12.0**
Predicted Range			**1.4 - 1.7**	**2.8 - 3.4**	**28 - 33**	**280 - 330**

Device	Length (μm)	Width (μm)	Speed (μm/sec) 100 Hz	1 kHz	10 kHz
12	100	60	2.5	22	183
13	100	80	3.6	34	316
14	100	80	2.5		
15	100	80	2.7	28	285
16	100	80	4.1	27	265
17	100	80	3.7	37	313
18	100	80	3.1	31	
Mean			**3.2**	**29.8**	**272.4**
Std. Dev.			**0.6**	**5.3**	**54.2**
Predicted Range			**3.1 - 3.7**	**31 - 37**	**310 - 370**

Table 1.2. Maximum speed for high-frequency drive signals. Left: Plate Voltage = 50 V. Right: Plate Voltage = 60 V.

Device	Length (μm)	Width (μm)	Speed (μm/sec) 10 kHz	100 kHz
8	100	80	327	
9	100	80	423	
10	100	80		1635
Mean			**375.0**	**1635**
Std. Dev.			**67.9**	**N/A**
Predicted Range			**280 - 330**	**2800 - 3300**

Device	Length (μm)	Width (μm)	Speed (μm/sec) 10 kHz	100 kHz
12	100	60	264	
13	100	80	286	
14	100	80	387	488†
15	100	80	386	553†
16	100	80	479	
17	100	80	474	1947
19	100	80		1825
Mean			**379.3**	**1886**
Std. Dev.			**90.6**	**86.3**
Predicted Range			**310 - 370**	**3100 - 3700**

†These data points correspond to measurements in which the actuators travelled off of their electrodes onto (much thinner) wires that supply power to the main electrodes. They are not included in the mean and standard deviation.

To measure the speed of these devices, we used a function generator and an amplifier to apply 100 V and 120 V square wave signals between adjacent electrodes, at frequencies of 50 Hz, 100 Hz, 1 kHz, and 10 kHz. This results in 50 V and 60 V potentials between the actuator plate and any of the underlying electrodes, as discussed in Section 1.3. (During these experiments, the underlying substrate was held at ground potential.) The motion of the devices under these control waveforms was filmed with a video camera[2], and the video frames were extracted as still images. Inter-frame motion estimates were then used to determine the speed of the actuators based on the frame rate of the video. The resulting data are shown in Table 1.1 and Figure 1.6. The average step size of the actuators, Δx, can be calculated from the ratio of the actuator speed to the frequency of the waveform.

At frequencies near 100 kHz, the motion of the actuators occurs in short, sporadic bursts on the order of a tenth of a second. So, it is more appropriate to measure the maximum speed between any two adjacent frames of the video than to take an average speed across many frames. Data taken in this fashion for actuators driven at 10 kHz and 100 kHz appear in Table 1.2 and in Figure 1.6.

From the measured speed of an actuator and the frequency of the applied waveform, we can calculate the average step size during travel. A scratch drive actuator's step size can be modelled analytically as follows [30]:

$$\Delta x = P\sqrt{V} \tag{1.2}$$

[2] Video was taken with both analog and digital cameras, and was then imported for analysis and processing with Adobe Premiere and Matlab.

where P is a constant defined by:

$$P = \left(\frac{27k\epsilon_0 h^6}{4Edt^3} \right)^{1/4} \tag{1.3}$$

in which k is the dielectric constant, ϵ_0 is the permittivity of free space, h is the bushing height, E is the Young's modulus of the plate material, d is the thickness of the insulating layer, and t is the thickness of the scratch drive plate.

To calculate the expected step size for the actuators used in this experiment, we need to know the thickness of the insulating oxide layer (d). While ellipsometric measurements of test wafers give us an approximation of the oxide thickness on the top of the electrodes (500 Å), the oxide on the underside of the actuators grows at a slower rate, due to restricted gas transport through the small channel between the actuator and the substrate. Since the total insulator thickness, d, is the the sum of these two layers, we modelled the thickness to lie between 500 and 1000 Å. For actuators driven at 50 V, this predicts a step size between 28 and 33 nm. For actuators driven at 60 V, the range is from 31 to 37 nm. The observed values fell near this predicted range, and are shown in Table 1.1.

The actuators achieved speeds of over 300 μm/s at drive frequencies of 10 kHz. At higher frequencies, even higher speeds were observed. At 100 kHz, the maximum drive frequency allowed by the voltage source, actuators were observed to exceed speeds of 1.5 mm/sec (Table 1.2).

Video of these untethered actuators can be viewed on the internet at:
`www.cs.dartmouth.edu/~brd/Research/MEMS/Movies/`

8 Conclusions

This work provides basic components that enable untethered locomotion at the MEMS scale. We provide a power delivery mechanism that is independent of device location and orientation, an automated release process, and a microfabrication process for building untethered devices. We have demonstrated the feasibility of these components through the development of untethered scratch drive actuators, and have characterized the performance of these devices.

In the course of producing untethered scratch drive actuators, we have developed a novel post-processing technique for *post hoc* insertion of dielectric layers between previously-deposited polysilicon films. We have successfully employed this technique to insulate devices fabricated with the PolyMUMPS process.

We hope that the techniques presented in this paper will be valuable for future work on autonomous locomotion of MEMS devices. Given the ability to locomote freely on the substrate, the natural next step is to devise steering mechanisms and control systems for untethered MEMS actuators. Work is underway in our laboratory to pursue this goal.

Acknowledgements. This work was supported by award no. 2000-DT-CX-K001 from the Office for Domestic Preparedness (U. S. Department of Homeland Security), National Science Foundation grants EIA-0202789, EIA-9901589, IIS-9906790, EIA-0102710, EIA-0102712, EIA-9818299, EIA-9802 068, EIA-0305444, and IIS-9912193, a NASA Spacegrant, and Microsoft Research. Devices were fabricated in part through the PolyMUMPs process at Cronos Integrated Microsystems, and were later wire-bonded at the Micro-Technology Lab of the Massachusetts Institute of Technology. The motion estimation code for measuring

actuator speed was generously provided by Hany Farid and Senthil Periaswamy. We thank Charlie Sullivan for the use of bench space in his lab; Laura Ray for the use of her Piezo Amplifier; and Chuck Daghlian and the Rippel Electron Microscopy Lab for the use of their CO_2 critical-point drying system, their SEM, and their many helpful suggestions. Finally, many thanks to Karl Bohringer, Zack Butler, Igor Paprotny, and Keith Kotay for their advice and discussions.

References

1. T. Akiyama and K. Shono, “Controlled stepwise motion in polysilicon microstructures,” *Journal of Microelectromechanical Systems*, vol. 2, no. 3, pp. 106–110, September 1993.
2. T. Akiyama, D. Collard, and H. Fujita, “Scratch drive actuator with mechanical links for self-assembly of three-dimensional MEMS,” *Journal of Microelectromechanical Systems*, vol. 6, no. 1, pp. 10–17, March 1997.
3. S. Baglio, S. Castorina, L. Fortuna, and N. Savalli, “Development of autonomous, mobile micro-electro-mechanical devices,” in *IEEE International Symposium on Circuits and Systems. Proceedings*, vol. IV, 2002, pp. 285–288.
4. ——, “Technologies and architectures for autonomous "MEMS" microrobots,” in *IEEE International Symposium on Circuits and Systems. Proceedings*, vol. II, 2002, pp. 584–587.
5. P. Basset, A. Kaiser, P. Bigotte, D. Collard, and L. Buchaillot, “A large stepwise motion electrostatic actuator for a wireless microrobot,” in *Proceedings of the IEEE International Conference on Micro Electro Mechanical Systems*, 2002, pp. 606–609.
6. P. Dario, R. Valeggi, M. C. Carrozza, M. C. Montesi, and M. Cocco, “Microactuators for microrobots: a critical survey,” *Journal of Micromechanics and microengineering*, p. 141, September 1992.
7. T. Ebefors, J. U. Mattsson, E. Kälvesten, and G. Stemme, “A walking silicon micro-robot,” *Transducers*, pp. 1202–1205, June 1999.
8. H. Fujita, “A decade of mems and its future,” in *Proceedings of the IEEE International Conference on Micro Electro Mechanical Systems*, 1996, pp. 1–7.
9. T. Fukuda, H. Hosokai, H. Ohyama, H. Hashimoto, and F. Arai, “Giant magnetostrictive alloy (GMA) applications to micro mobile robot as a micro actuator without cables,” in *Proceedings of the IEEE International Conference on Micro Electro Mechanical Systems*, 1991, pp. 210–215.
10. K. Ioi, “A mobile micro-robot using centrifugal forces,” in *Proceedings of the IEEE International Conference on Advanced Intelligent Mechatronics*, September 1999, pp. 736–741.
11. ——, “Study on turning motion of micro robot driven by cyclic force,” in *Proceedings of the IEEE International Conference on Advanced Intelligent Mechatronics*, July 2001, pp. 1319–1324.
12. P. E. Kladitis and V. M. Bright, “Prototype microrobots for micro-positioning and micro-unmanned vehicles,” *Sensors and Actuators A (Physical)*, vol. A80, no. 2, pp. 132–137, March 2000.
13. R. J. Linderman and V. M. Bright, “Optimized scratch drive actuator for tethered nanometer positioning of chip-sized components,” in *Technical Digest. Solid-State Sensor and Actuator Workshop*, June 2000, pp. 214–217.
14. H. Miura, T. Yasuda, Y. K. Fujisawa, and I. Shimoyama, “Insect-model based microrobot,” in *Transducers*, June 1995, pp. 392–395.

15. M. H. Mohebbi, M. L. Terry, K. F. Bohringer, G. T. A. Kovacs, and J. W. Suh, "Omnidirectional walking microrobot realized by thermal microactuator arrays," in *Proceedings of the ASME. International Mechanical Engineering Congress and Exposition*, November 2001, pp. 1–7.
16. K. Rochdi and S. Dembele, "Static behavior of a piezoelectric micro robot," in *Proceedings of the IEEE Conference on Nanotechnology*, October 2001, pp. 180–184.
17. J. Seyfried, S. Fatikow, S. Fahlbusch, A. Buerkle, and F. Schmoeckel, "Manipulating in the micro world: Mobile micro robots and their applications," in *Proceedings of the 31st International Symposium on Robotics*, May 1999, pp. 3–9.
18. F. Schmoeckel and H. Worn, "Remotely controllable mobile microrobots acting as nano positioners and intelligent tweezers in scanning electron microscopes (SEMs)," in *Proceedings of the IEEE International Conference on Robotics and Automation*, 2001, pp. 3909–3913.
19. K. Suzuki, I. Shimoyama, and H. Miura, "Insect-model based microrobot with elastic hinges," *Journal of Microelectromechanical Systems*, vol. 3, no. 1, pp. 4–9, March 1994.
20. M. Takeda, "Application of mems to industrial inspection," in *Proceedings of the IEEE International Conference on Micro Electro Mechanical Systems*, 2001, pp. 182–191.
21. H. Worn, F. Schmoeckel, A. Buerkle, J. Samitier, M. Puig-Vidal, S. Johansson, U. Simu, J.-U. Meyer, and M. Biehl, "From decimeter- to centimeter-sized mobile microrobots – the development of the miniman system," in *Proceedings of the SPIE. Microrobotics and Microassembly III*, vol. 4568, 2001, pp. 175–186.
22. T. Yasuda, I. Shimoyama, and H. Miura, "Microrobot actuated by a vibration energy field," *Sensors and Actuators A*, vol. 43, pp. 366–370, 1994.
23. R. Yeh, E. J. J. Kruglick, and K. S. J. Pister, "Surface-micromachined components for articulated microrobots," *Journal of Microelectromechanical Systems*, vol. 5, no. 1, pp. 10–17, March 2001.
24. E. W. H. Jager, O. Inganäs, and I. Lundström, "Microrobots for micrometer-size objects in aqueous media: Potential tools for single-cell manipulation," *Science*, vol. 288, no. 5475, pp. 2335–2338, June 2000.
25. M. Mason, *Mechanics of Robotic Manipulation*. Cambridge, MA: MIT Press, 2001.
26. B. R. Donald, J. Jennings, and D. Rus, "Information invariants for distributed manipulation," International Journal of Robotics Research, vol. 16, no. 5, pp. 673 – 702, 1997.
27. B. R. Donald *et al.*, *Algorithmic and Computational Robotics: New Directions*. Boston, MA: A. K. Peters, 2001, Meso-Scale Self-Assembly, by D. H. Gracias *et al.*, pp. 1-8.
28. K. Kotay and D. Rus, "Locomotion versatility through self-reconfiguration," *Robotics and Autonomous Systems*, vol. 26, pp. 217–32, 1999.
29. K. W. Markus, D. A. Koester, A. Cowen, R. Mahadevan, V. R. Dhuler, D. Roberson, and L. Smith, "MEMS infrastructure: The multi-user MEMS processes (MUMPs)," in *Proceedings of the SPIE - The International Society for Optical Engineering, Micromachining and Microfabrication Process Technology*, vol. 2639, 1995, pp. 54–63.
30. K. Hayakawa, A. Torii, and A. Ueda, "An analysis of the elastic deformation of an electrostatic microactuator," *Transactions of the Institute of Electrical Engineers of Japan, Part E*, vol. 118-E, no. 3, pp. 205–211, March 1998.
31. N. Finch, J. Marchetti, H. Fujita, and J. Guoy, "CAD modeling of scratch drive actuation," in *Proceedings of the SPIE. Design, Modeling, and Simulation in Microelectronics*, vol. 2639, 2000, pp. 83–89.
32. L. G. Frechette, S. F. Nagle, R. Ghodssi, S. D. Umans, M. A. Schmidt, and J. H. Lang, "An electrostatic induction micromotor supported on gas-lubricated bearings," in *14th IEEE International Conference on Micro Electro Mechanical Systems*, 2001, pp. 290–293.

33. A. Buerkle, F. Schmoeckel, M. Kiefer, B. P. Amavasai, F. Caparrelli, A. N. Selvan, and J. R. Travis, “Vision-based closed-loop control of mobile microrobots for micro handling tasks,” in *Proceedings of the SPIE. Microrobotics and Microassembly III*, vol. 4568, 2001, pp. 187–198.
34. C. Cassier, A. Ferreira, and S. Hirai, “Combination of vision servoing techniques and vr-based simulation for semi-autonomous microassembly workstation,” in *Proceedings of the IEEE International Conference on Robotics and Automation*, May 2002, pp. 1501–1506.
35. S. Fatikow and U. Rembold, “An automated microrobot-based desktop station for micro assembly and handling of microobjects,” in *Proceedings of the IEEE International Conference on Micro Electro Mechanical Systems*, September 1996, pp. 586–592.
36. S. Fatikow, J. Seyfried, S. Fahlbusch, A. Buerkle, and F. Schmoeckel, “A flexible microrobot-based microassembly station,” in *Proceedings of the IEEE International Conference on Emerging Technologies and Factory Automation*, 1999, pp. 397–406.
37. I. W. Hunter, S. Lafontaine, P. M. F. Nielsen, P. J. Hunter, and J. M. Hollerbach, “Manipulation and dynamic mechanical testing of microscopic objects using a tele-micro-robot system,” in *Proceedings of the IEEE International Conference on Robotics and Automation*, May 1989, pp. 3–9.
38. T. Kasaya, Hideki, Miyazaki, S. Saito, and T. Sato, “Micro object handling under SEM by vision-based automatic control,” in *Proceedings of the IEEE International Conference on Robotics and Automation*, May 1999, pp. 2189–2196.
39. L. Luming and W. Liding, “Micromanipulator system in mems,” in *Proceedings of the IEEE International Conference on Industrial Technology*, 1996, pp. 665–668.
40. S. Martel, P. Madden, L. Sosnowski, I. Hunter, and S. Lafontaine, “Nanowalker: A fully autonomous highly integrated miniature robot for nano-scale measurements,” in *Proceedings of the SPIE. Microsystems Metrology and Inspection*, vol. 3825, 1999, pp. 111–122.
41. M. Rodriguez and A. Codourey, “Graphical user interface to manipulate objects in the micro world with a high precision robot,” in *Proceedings of the IEEE International Conference on Robotics and Automation*, April 1997, pp. 3031–3036.
42. B. E. Deal and A. S. Grove, “General relationship for the thermal oxidation of silicon,” *Journal of Applied Physics*, vol. 36, no. 12, pp. 3770–3778, December 1965.
43. S. K. Ghandhi, *VLSI fabrication principles : silicon and gallium arsenide*, 2nd ed. Wiley-Interscience, 1994, pp. 501,576.
44. L. Li, J. G. Brown, and D. Uttamchandani, “Detailed study of scratch drive actuator characteristics using high-speed imaging,” in *Proceedings of the SPIE. Reliability, Testing, and Characterization of MEMS/MOEMS*, vol. 4558, 2001, pp. 117–123.
45. G. Lucovsky, M. J. Manitini, J. Srivastava, and E. A. Irene, “Low-temperature growth of silicon dioxide films: A study of chemical bonding by ellipsometry and infrared spectroscopy,” *Journal of Vacuum Science and Technology B (Microelectronics processing and phenomena)*, vol. 5, no. 2, pp. 530–537, March-April 1987.